CHALMERS
UNIVERSITY OF TECHNOLOGY

Evaluation and Comparison of Small-Signal Characteristics of Grid-Forming Converter Systems in Two Different Reference Frames

Citation for the original published paper (version of record):
Narula, A., Bongiorno, M., Mattavelli, P. et al (2025). Evaluation and Comparison of Small-Signal Characteristics of Grid-Forming Converter Systems in
Two Different Reference Frames. IEEE Open Journal of Industry Applications, 6: 206-220.
http://dx.doi.org/10.1109/OJIA.2025.3564501

(article starts on next page)

IEEE Open Journal of
Industry Applications

Received 8 November 2024; revised 2 March 2025; accepted 17 April 2025. Date of publication 25 April 2025;
date of current version 7 May 2025.

Digital Object Identifier 10.1109/OJIA.2025.3564501

Evaluation and Comparison of Small-Signal Characteristics of Grid-Forming Converter Systems in Two Different Reference Frames

ANANT NARULA [1] (Member, IEEE), MASSIMO BONGIORNO [1] (Senior Member, IEEE), PAOLO MATTAVELLI [2] (Fellow, IEEE), MEBTU BEZA [1] (Member, IEEE), JAN R. SVENSSON [3] (Senior Member, IEEE), AND WENTAO LIU [1] (Member, IEEE)

[1]Department of Electrical Engineering, Chalmers University of Technology, 41296 Göteborg, Sweden
[2]Department of Management and Engineering, University of Padova, 36100 Vicenza, Italy
[3]Hitachi Energy Research, 72226 Västerås, Sweden

CORRESPONDING AUTHOR: ANANT NARULA (email: anant.narula@chalmers.se).

This work was supported in part by the Swedish Electricity Storage and Balancing Centre (SESBC), and is in collaboration with the CETPartnership project WIND-DIGIPOWER, SESBC is funded by the Swedish Energy Agency together with five academic and 28 nonacademic partners.

ABSTRACT The increasing penetration of converter-interfaced generation units results in a frequency-weak power system characterized by decreasing system inertia. Consequently, the angular frequency of the power system may deviate from its nominal value, with its dynamics significantly influenced by the various control loops of converters. To accurately conduct small-signal analysis of such power systems, two impedance-based modeling approaches have been proposed in recent years. The first approach derives small-signal models in a synchronously rotating reference frame, also referred to as the *dq*-frame, which is defined by the power system's nominal angular frequency. This method characterizes individual converter systems using only their *dq*-domain impedance matrix. The second approach, on the other hand, develops small-signal models in a *dq*-frame defined by the dynamic angular frequency of the power system. In this case, converter systems are characterized not only by their *dq*-impedance matrix but also by an additional transfer matrix that relates variations in the output current to variations in the power system's angular frequency. This leads to different closed-loop transfer matrices for the two approaches, which are used to assess small-signal stability. This article shows, using the derived analytical models, that despite the differences in the closed-loop transfer matrices, the two impedance-based modeling approaches are equivalent and lead to the same conclusions regarding the small-signal stability of the overall system. However, the second approach offers better physical insight into the behavior of converter systems during disturbances. Experimental results are provided to validate the theoretical analysis.

INDEX TERMS Frequency dynamics, grid-forming (GFM) system, impedance model, small-signal analysis, voltage-source converters (VSCs).

NOMENCLATURE

List of Symbols

R_g	Resistance of the grid (Ω).
L_g	Inductance of the grid (H).
$\hat{X}_g$	Estimated reactance of the grid (Ω).
R_f	Resistance of the converter filter (Ω).
L_f	Inductance of the converter filter (H).
X_f	Reactance of the converter filter (Ω).
e_s	3-Φ voltage at terminal of ideal voltage source (V).
E_s	Rms value of the line-to-line source voltage (V).
ω_s	Angular frequency of the source voltage (rad/s).
θ_s	Source voltage angle (rad).
e_g	3-Φ voltage at point-of-common-coupling, PCC (V).
E_g	Rms value of the line-to-line voltage at the PCC (V).

ω_g Angular frequency of the PCC voltage (rad/s).
θ_g PCC voltage angle (rad).
e_c 3-Φ voltage at converter's terminal (V).
E_c Rms value of the line-to-line converter voltage (V).
ω_c Angular frequency of the converter voltage (rad/s).
θ_c Converter voltage angle (rad).
i_f 3-Φ current across the converter filter (A).
i_g 3-Φ current across the grid impedance (A).
P_c 3-Φ active power output of the converter (W).
Q_c 3-Φ reactive power output of the converter (VAr).
P_g 3-Φ active power injected to the grid (W).
Q_g 3-Φ reactive power injected to the grid (VAr).
S_N Rated power of the converter (VA).
E_N Rated line-to-line voltage of the system (V).
ω_N Rated angular frequency of the system (rad/s).
H Inertia time-constant of the grid (s).
K_D Mechanical damping coefficient of the grid (per unit).
s Laplace transform variable (rad/s).
R'_a Active resistance used in ac voltage controller (Ω).
α_{hpf} Cutoff frequency of the high-pass filter (rad/s).
α_{vc} Loop-bandwidth of the ac voltage controller (rad/s).
$K_{i,vc}$ Gain of the integrator in ac voltage controller (rad/s).
$K_{p,pc}$ Active power controller's proportional gain (rad/s).
$K_{i,pc}$ Active power controller's integral gain (rad^2/s^2).
R_a Active damping term in active power controller (rad/s).
K_s Synchronizing power coefficient (W).
α_{pc} Loop-bandwidth of the active power controller (rad/s).
α_{lpf} Cutoff frequency of the low-pass filter (rad/s).
θ_L Load angle of the converter in dq^{ω_N} frame (rad).
θ'_L Load angle of the voltage source in dq^{ω_N} frame (rad).
δ_L Load angle of the converter in dq^{ω_g} frame (rad).
δ'_L Load angle of the voltage source in dq^{ω_g} frame (rad).

Conventions Used

Superscript "$\star$" denotes a reference signal.

Superscripts "ω_c," "ω_s," "ω_N," and "ω_g" indicate quantities in the converter dq-frame, source dq-frame, dq^{ω_N} frame, and dq^{ω_g} frame, respectively.

Subscripts "d" and "q" represent the d- and q-components of a space vector in the corresponding dq-frame.

Symbol "Δ" preceding a variable denotes its perturbation component.

Subscript "0" signifies steady-state quantities.

Bold variables represent matrices.

I. INTRODUCTION

Aligning with global efforts to achieve carbon neutrality and foster a sustainable energy future, there is a continuous growth of renewable energy generation. To ensure controllability and flexibility, renewable energy sources are commonly interfaced to the grid by power-electronic devices, such as voltage-source converters (VSCs). Consequently, the proportion of renewables and power electronics in modern electric power systems has increased significantly and is projected to rise even further in the future [1]. However, an increase in the penetration level of converter-interfaced generation technologies introduces new oscillation modes and alters the dynamic behavior of power systems following disturbances [1], [2]. This brings the need for methodologies that accurately capture the dynamics introduced by converter technologies, as well as new stability assessment tools to ensure the reliable and stable operation of modern power systems under evolving grid conditions.

Small-signal stability assessment of power electronics-dominated power systems (PEDPS) can be conducted using both time-domain and frequency-domain methods. Time-domain methods primarily include eigenvalue analysis based on detailed state–space models. A key advantage of eigenvalue analysis using state–space models is its ability to identify oscillation modes and the participation factors of system and control parameters [3]. However, the main limitation is that detailed system and controller information for converter systems is typically required, which may not be feasible in real-world scenarios [4], [5], [6]. In addition, the complexity and computational burden increase significantly for large networks, making time-domain approaches less suitable for small-signal analysis [7], [8].

To address the limitations of time-domain methods, frequency-domain approaches are a suitable choice for performing small-signal analysis of PEDPS. In particular, the impedance-based approach has emerged as an effective method for modeling and analyzing the small-signal characteristics of converter systems [7], [8], [9], [10], [11]. Impedance models represent individual converter systems in terms of their frequency-dependent impedances, which allows for a modular approach to analyzing complex interconnected systems. This modularity simplifies the assessment of the interaction between converter systems without requiring detailed knowledge of their internal states. For instance, Wang et al. [8] employed an impedance-based approach in a three-phase meshed network to analyze harmonic instability caused by interactions between the inner control loops of voltage- and current-controlled inverters, while Tan et al. [9] applied the impedance-based method for stability analysis of VSC-HVDC systems.

Impedance-based small-signal stability analysis can be conducted in either the stationary $\alpha\beta$-reference frame or the synchronously rotating dq-reference frame [10], [11]. In this approach, a power system is typically decomposed into source and load subsystem equivalents. Small-signal stability is then assessed using methods, such as generalized Nyquist criterion [12], [13], [14], [15], passivity [16], [17], [18], [19], [20], [21], and positive-net-damping [22], [23], [24], [25]. Each of these methods has its strengths and weaknesses, and their applicability depends on the specific system and phenomenon being analyzed. For example, while the generalized Nyquist criterion can characterize resonances in a system [13] and determine overall system stability [15], it does not always provide direct insight into the root causes of

instability. On the other hand, passivity-based analysis helps identify the contribution of individual subsystems to overall stability [18], [19] and aids in designing converter control strategies to mitigate adverse system interactions [16], [17], [20], [21]. However, its conservative nature can lead to overly strict assessments, potentially resulting in false instability predictions.

Despite advancements in impedance-based analysis of power systems, most studies assume that the power system's angular frequency remains constant when modeling subsystems. However, with the increasing penetration of converter-interfaced generation units, power systems are becoming frequency-weaker due to reduced system inertia and the introduction of new dynamics by converter systems. Consequently, variations in the system's angular frequency can no longer be neglected. Several studies have investigated the inclusion of frequency dynamics in small-signal models [26], [27], [28], [29], [30], [31], [32]. The studies in [26], [27], [28], [31], and [32] propose small-signal modeling in a synchronously rotating *dq*-frame (SRF) defined by the angular frequency of the voltage at the point-of-common-coupling (PCC), which is considered as the system's fundamental angular frequency. Using this approach, small-signal characteristics of converter systems are modeled not only with their *dq*-impedance matrix but also with a transfer matrix that correlates variations in the converter system's output current to variations in the fundamental angular frequency. While using this type of approach introduces an additional step in the small-signal stability assessment compared to the conventional *dq*-impedance-based method, it offers better physical insights into the dynamic behavior of converter systems during grid disturbances, including variations in grid voltage magnitude and frequency [29]. Conversely, the study in [30] establishes small-signal models in a *dq*-frame defined by the system's rated angular frequency. It further shows that, in this context, the effects of fundamental frequency variations are inherently incorporated within the terminal *dq*-impedance matrix of converter systems, enabling the application of conventional impedance-based small-signal stability assessment criteria. However, the mathematical relationship between impedance models in the two reference frames remains unclear in the existing literature. Furthermore, it has not yet been addressed whether the choice of reference frame influences small-signal stability analysis.

To address this gap, this article mathematically and comprehensively explores the similarities and differences between the impedance-based modeling approaches of converter systems in the two types of SRFs. It demonstrates that these two modeling approaches for converter systems are mathematically equivalent and provide the same conclusions regarding the small-signal stability of the overall system. Furthermore, the key advantages and disadvantages of each approach are highlighted. Finally, experimental tests of a grid-connected converter system are conducted to validate the theoretical findings.

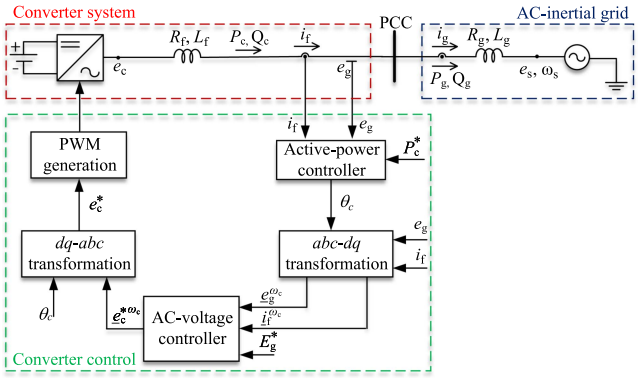

FIGURE 1. Single-line diagram of considered grid-connected converter system and block scheme of implemented GFM control.

II. SYSTEM AND CONTROLLER DESCRIPTION

Fig. 1 shows the single-line diagram of a grid-connected converter system together with the block scheme of the implemented controller. The grid model consists of an ideal voltage source behind a grid impedance, with resistance R_g and inductance L_g. The three-phase voltage at the voltage source is denoted by e_s, while the voltage at the PCC and the converter's terminal are denoted by e_g and e_c, respectively. The quantities P_c and Q_c represent the active and reactive power output of the converter system; whereas, P_g and Q_g are the active and reactive power injected to the grid, respectively. The variables i_f and i_g denote the three-phase current across the converter filter and the grid, respectively. For the considered system, $P_c = P_g$, $Q_c = Q_g$, and $i_f = i_g$. The magnitude of the source voltage, E_s, is assumed constant; whereas, to account for inertia and to model frequency dynamics in the grid, the angular frequency of the voltage source, ω_s, is obtained using the swing equation as follows [33]:

$$\omega_s = \overbrace{\left(\frac{1}{\frac{2H}{\omega_N}s + \frac{K_D}{\omega_N}}\right)}^{G'_{pc}} \frac{(P_g - P_g^\star)}{S_N} + \omega_N. \tag{1}$$

The terms S_N and ω_N denote the base power (here the rated power of the converter is selected as the base value) and rated angular frequency of the system, respectively. H and K_D represent the inertia time-constant (in seconds) and mechanical damping coefficient (in per unit) of the grid, respectively. The term s is the Laplace-transform variable, interpreted as d/dt where appropriate, and "$\star$" denotes a reference signal in the notations.

A grid-forming (GFM) control strategy is implemented for the converter system, utilizing the direct control of converter voltage (DCCV) approach described in [34]. It is important to note that this particular GFM control strategy has been chosen for its simplicity; however, the analysis presented in this article is independent of the specific type of control strategy used for the converter system. In DCCV approach, an ac

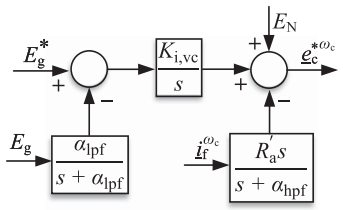

FIGURE 2. Block scheme of implemented AVC in converter system.

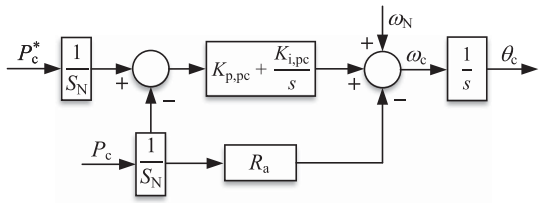

FIGURE 3. Block scheme of implemented APC in converter system.

voltage controller[1] (AVC) regulates the magnitude of the voltage at the PCC and calculates the reference value of the converter voltage magnitude, $E_c^\star$, while an active power controller (APC) calculates the converter voltage angle, θ_c. To enable fault-ride-through capability, an embedded current controller is typically included in this control strategy. This controller remains inactive during normal operation but activates when overcurrent conditions arise [35], [36]. However, since the primary focus of this study is on small-signal stability, current limitation scenarios are not considered, and thus, the current controller is not shown in Fig. 1 as well as excluded from the system model in the following. Furthermore, all controllers are designed in the converter dq-frame (using power-invariant transformation), which is defined by the angle output of the APC.

As depicted in Fig. 2, the AVC implemented here comprises of a pure integrator. Accordingly, the reference value for the converter voltage vector, $\underline{e}_c^{\star\omega_c}$, is calculated as follows [34]:

$$\underline{e}_c^{\star\omega_c} = E_N + \overbrace{\frac{K_{i,vc}}{s}}^{G_{vc}}\left(E_g^\star - \overbrace{\frac{\alpha_{lpf}}{s+\alpha_{lpf}}}^{G_{lpf}} E_g\right) - \overbrace{\frac{s}{s+\alpha_{hpf}}}^{G_{hpf}} R_a' \underline{i}_f^{\omega_c} \quad (2)$$

where E_N denotes the rated line-to-line voltage of the system and E_g denotes magnitude of the measured line-to-line voltage at the PCC. The superscript "ω_c" is used to represent quantities in the converter dq-frame. The term α_{lpf} denotes the cutoff frequency of the low-pass filter for the PCC voltage measurement. A transient damping term comprising the high-pass filtered converter current is added at the output of the AVC to prevent a poorly damped closed-loop response. R_a' denotes the active resistance, and α_{hpf} the cutoff frequency of the high-pass filter, with values selected as suggested in [34]. The integral gain of the controller, $K_{i,vc}$, can be calculated using the loop-shaping approach as, $K_{i,vc} = \frac{\alpha_{vc}(X_f+\hat{X}_g)}{(\hat{X}_g)}$, where α_{vc} denotes the desired closed-loop bandwidth (in rad/s) of the first-order response from $E_g^\star$ to E_g. X_f and $\hat{X}_g$ denote the reactance corresponding to the filter inductance L_f and estimated grid inductance, respectively. To guarantee the desired response speed for all grid conditions, $\hat{X}_g$ is typically set for the strongest grid strength provided by the system operator [34].

[1] Alternatively, a reactive power controller can be used, depending on the system's requirements

For the investigated GFM control, the APC provides both active-power reference tracking and grid synchronization. The implemented APC consists of a proportional–integral regulator for accurate reference tracking and an active damping term, R_a, to improve the controller's dynamic performance. As depicted in Fig. 3, the APC calculates the converter voltage angle as [34]

$$\theta_c = \frac{1}{s}\omega_c = \frac{1}{s}\left[\overbrace{\left(K_{p,pc}+\frac{K_{i,pc}}{s}\right)}^{G_{pc}}\frac{(P_c^\star - P_c)}{S_N} - R_a\frac{P_c}{S_N} + \omega_N\right]. \quad (3)$$

The control parameters of the APC are tuned using the loop-shaping approach to obtain a first order closed-loop response from $P_c^\star$ to P_c. Accordingly, $K_{p,pc} = \frac{\alpha_{pc}}{K_s}S_N$, $K_{i,pc} = \frac{\alpha_{pc}^2}{K_s}S_N$, and $R_a = K_{p,pc}$, where α_{pc} is the loop bandwidth (in rad/s) of the APC. The synchronizing power coefficient is given by $K_s = \frac{E_c E_s}{(X_f+\hat{X}_g)}$.

III. SYNCHRONOUS REFERENCE FRAMES DEFINITIONS

To derive a small-signal model of the overall system, all circuit variables must be transformed to one common SRF, referred to in this article as the system dq-frame. This section defines the two types of system dq-frames used to obtain the small-signal models of the grid-connected converter system. 1) dq^{ω_N} frame: In this frame, the d^{ω_N} and q^{ω_N} axes rotate at the system's rated angular frequency, ω_N. 2) dq^{ω_g} frame: This frame is aligned with the PCC voltage, meaning that the d^{ω_g} and q^{ω_g} axes rotate at the angular frequency of the PCC voltage, ω_g.

A. SYSTEM DQ-FRAME I

The first type of system dq-frame considered here, denoted as the dq^{ω_N} frame (represented by d^{ω_N}, q^{ω_N} axes in Fig. 4), is defined by the transformation angle, θ_N, which is obtained by integrating ω_N, i.e., $\theta_N = \frac{\omega_N}{s}$. Since the dq^{ω_N} frame rotates with ω_N, the d^{ω_N} and q^{ω_N} axes do not oscillate under small-signal perturbations. On the other hand, in accordance with (1) and (3), under small-signal perturbations resulting in power variations, the converter dq-frame (rotating with ω_c and represented by d^{ω_c}, q^{ω_c} axes in Fig. 4) and the source dq-frame (rotating with ω_s and represented by d^{ω_s}, q^{ω_s} axes

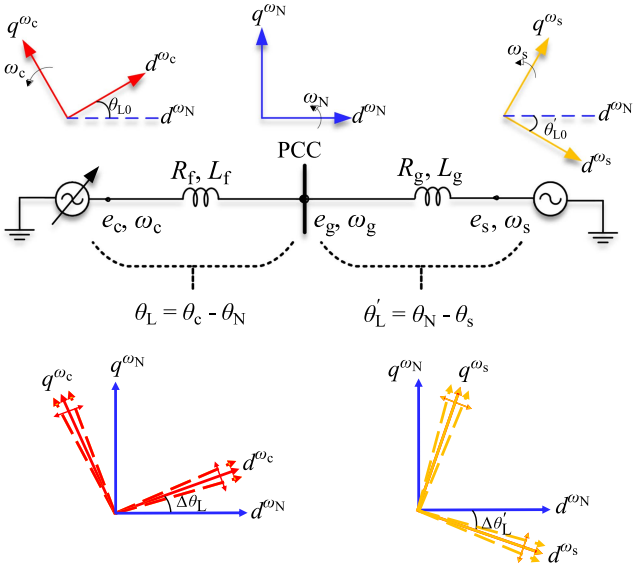

FIGURE 4. Illustration of dq^{ω_N} frame, converter dq-frame, and source dq-frame alignments during steady state (top figure) and under small-signal perturbations (bottom figure).

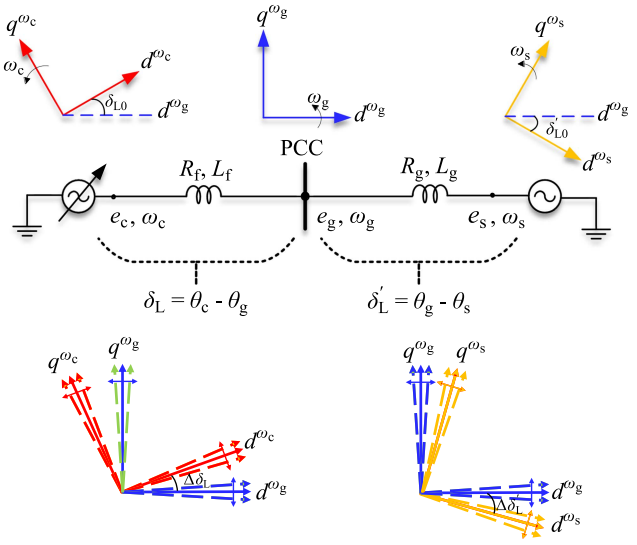

FIGURE 5. Illustration of dq^{ω_g} frame, converter dq-frame, and source dq-frame alignments during steady state (top figure) and under small-signal perturbations (bottom figure).

in Fig. 4), oscillate around their respective steady-state positions. As shown in the figure, the angle difference between the converter dq-frame and the dq^{ω_N} frame, also known as the converter load angle, is denoted by θ_L in Fig. 4. Similarly, θ'_L represents the angle difference between the dq^{ω_N} frame and the source dq-frame, also referred to as the load angle of the voltage source. The steady-state load angles of the converter and voltage source with respect to dq^{ω_N} frame, denoted as θ_{L0} and θ'_{L0}, respectively, are determined by the load flow analysis of the network. Furthermore, $\Delta\theta_L$ and $\Delta\theta'_L$ describe the variations in the corresponding load angles during small-signal perturbations. Since the dq^{ω_N} frame does not oscillate during small-signal perturbations, $\Delta\theta_L$ and $\Delta\theta'_L$ are solely governed by variations in the converter-voltage angle and the source-voltage angle, respectively, as described in Section IV.

B. SYSTEM DQ-FRAME II

The second SRF considered here, denoted as the dq^{ω_g} frame (represented by d^{ω_g} and q^{ω_g} axes in Fig. 5), is aligned to the PCC voltage. Accordingly, it is defined by the PCC voltage angle, θ_g, which is obtained by integrating the angular frequency, ω_g, of the three-phase voltage at the PCC, i.e., $\theta_g = \frac{\omega_g}{s}$. Unlike the dq^{ω_N} frame, small-signal perturbations resulting in active-power variations (and hence a perturbation in ω_g), cause the d^{ω_g} and q^{ω_g} axes to oscillate around their respective steady-state positions, as depicted in Fig. 5. The load angle of the converter in the dq^{ω_g} frame is denoted by δ_L in Fig. 5, while δ'_L denotes the load angle of the voltage source in the dq^{ω_g} frame. The steady-state load angles of the converter and voltage source with respect to dq^{ω_g} frame are given by δ_{L0} and δ'_{L0}, respectively, and are determined through the load-flow analysis. Due to the oscillation of dq^{ω_g} frame during small-signal perturbations, the variation in the converter load angle, $\Delta\delta_L$, is influenced by changes in both the converter-voltage angle and the PCC voltage angle. Similarly, the variation in the load angle of the voltage source, $\Delta\delta'_L$, depends on variations in both the source-voltage angle and the PCC voltage angle. These relationships are further detailed in the following section.

IV. SMALL-SIGNAL MODELING

The conventional impedance-based method is employed to define the small-signal characteristics of the grid-connected converter system under consideration. This frequency-domain method partitions the overall system into two subsystems: 1) the element under study, which in this case is the GFM converter, and 2) the remainder of the system, here constituted by the inertial grid [37]. Depending on the selected inputs and outputs, each subsystem is modeled using either its Thévenin or its Norton equivalent. Specifically, if voltages are chosen as inputs and currents as outputs, the subsystem is represented using a Norton equivalent. Conversely, if currents are selected as inputs and voltages as outputs, a Thévenin equivalent is used. The impedance-based modeling approach offers significant advantages over other small-signal stability analysis methods. Notably, it facilitates the independent analysis of subsystems, making it particularly effective for identifying potential resonance sources and paths in large-scale power systems with multiple interconnected converters [38].

In this section, analytical models describing the small-signal characteristics of the grid-connected converter system in two types of system dq-frame are derived. In addition, stability assessment criteria in each system dq-frame is established.

A. SMALL-SIGNAL MODEL IN SYSTEM DQ-FRAME I

In this section, the small-signal models of the converter system and the inertial grid in the dq^{ω_N} frame are first derived analytically and then validated through detailed time-domain simulations. Furthermore, using these small-signal models of individual subsystems, stability assessment criteria for the interconnected system are established.

1) SMALL-SIGNAL MODELING OF CONVERTER SYSTEM

To derive the small-signal model of the converter system in the dq^{ω_N} frame, the controller dynamics described previously should be transformed to this frame. By using (3), the angle θ_L is given as

$$\theta_L = \theta_c - \theta_N = \frac{1}{s}\frac{[G_{pc}(P_c^\star - P_c) - R_a P_c]}{S_N}. \tag{4}$$

Thus, any space-vector $\underline{z}^{\omega_c}$ defined earlier in the converter dq-frame can be transformed to the dq^{ω_N} frame using the following relation:

$$\underline{z}^{\omega_N} = \underline{z}^{\omega_c} e^{j\theta_L}. \tag{5}$$

Using linearized forms of (2), (4), and (5), the small-signal model of the converter voltage reference in the dq^{ω_N} frame can be expressed as

$$\begin{bmatrix}\Delta e_{cd}^{\star\omega_N}\\ \Delta e_{cq}^{\star\omega_N}\end{bmatrix} = \overbrace{\begin{bmatrix}-(e_{cq0}^{\omega_N} + G_{hpf}R_a' i_{fq0}^{\omega_N}) & G_{vc}\cos\theta_{L0}\\ (e_{cd0}^{\omega_N} + G_{hpf}R_a' i_{fd0}^{\omega_N}) & G_{vc}\sin\theta_{L0}\end{bmatrix}}^{\mathbf{G}_T}\begin{bmatrix}\Delta\theta_L\\ \Delta E_g^\star\end{bmatrix}$$
$$+\left(-\overbrace{\begin{bmatrix}\frac{G_{vc}G_{lpf}\cos\theta_{L0}e_{gd0}^{\omega_N}}{E_{g0}} & \frac{G_{vc}G_{lpf}\cos\theta_{L0}e_{gq0}^{\omega_N}}{E_{g0}}\\ \frac{G_{vc}G_{lpf}\sin\theta_{L0}e_{gd0}^{\omega_N}}{E_{g0}} & \frac{G_{vc}G_{lpf}\sin\theta_{L0}e_{gq0}^{\omega_N}}{E_{g0}}\end{bmatrix}}^{\mathbf{G}_{PVv1}}\right)\begin{bmatrix}\Delta e_{gd}^{\omega_N}\\ \Delta e_{gq}^{\omega_N}\end{bmatrix}$$
$$+\overbrace{\begin{bmatrix}-G_{hpf}R_a' & 0\\ 0 & -G_{hpf}R_a'\end{bmatrix}}^{\mathbf{G}_{DH}}\begin{bmatrix}\Delta i_{fd}^{\omega_N}\\ \Delta i_{fq}^{\omega_N}\end{bmatrix} \tag{6}$$

with

$$\begin{bmatrix}\Delta\theta_L\\ \Delta E_g^\star\end{bmatrix} = \begin{bmatrix}\frac{G_{pc}}{sS_N} & 0\\ 0 & 1\end{bmatrix}\begin{bmatrix}\Delta P_c^\star\\ \Delta E_g^\star\end{bmatrix}$$
$$+\overbrace{\begin{bmatrix}-\frac{(G_{pc}+R_a)e_{gd0}^{\omega_N}}{sS_N} & -\frac{(G_{pc}+R_a)e_{gq0}^{\omega_N}}{sS_N}\\ 0 & 0\end{bmatrix}}^{\mathbf{G}_{PVc2}}\begin{bmatrix}\Delta i_{fd}^{\omega_N}\\ \Delta i_{fq}^{\omega_N}\end{bmatrix}$$
$$+\overbrace{\begin{bmatrix}-\frac{(G_{pc}+R_a)i_{fd0}^{\omega_N}}{sS_N} & -\frac{(G_{pc}+R_a)i_{fq0}^{\omega_N}}{sS_N}\\ 0 & 0\end{bmatrix}}^{\mathbf{G}_{PVv2}}\begin{bmatrix}\Delta e_{gd}^{\omega_N}\\ \Delta e_{gq}^{\omega_N}\end{bmatrix} \tag{7}$$

where the expressions $P_c = e_{gd}^{\omega_N} i_{fd}^{\omega_N} + e_{gq}^{\omega_N} i_{fq}^{\omega_N}$, and $E_g = \sqrt{(e_{gd}^{\omega_N})^2 + (e_{gq}^{\omega_N})^2}$ are used for the active power output of the converter and the PCC-voltage magnitude, respectively. In general, (6) describes how variations in the converter load angle and set point for the AVC, PCC voltage, and converter current affect the converter's reference voltage. Equation (7) explains how variations in the converter's active power set point, and the actual active power variations at the PCC influence the converter load angle through the APC. The transfer matrices $\mathbf{G}_T$, $\mathbf{G}_{PVv1}$, and $\mathbf{G}_{DH}$ relate variations in the converter load angle and set point for the AVC, PCC voltage, and converter current, respectively, to variations in the reference voltage of the converter. Meanwhile, the transfer matrices $\mathbf{G}_{PVv2}$ and $\mathbf{G}_{PVc2}$ describe how variations in the PCC voltage and converter current, respectively, affect the converter load angle. The subscript "0" represents steady-state quantities in the notations.

By neglecting the impact of converter delays and using (6), (7), and the linearized expression for the current dynamics in the dq^{ω_N} frame, which is given by

$$\begin{bmatrix}\Delta e_{cd}^{\omega_N}\\ \Delta e_{cq}^{\omega_N}\end{bmatrix} = \begin{bmatrix}\Delta e_{gd}^{\omega_N}\\ \Delta e_{gq}^{\omega_N}\end{bmatrix} + \overbrace{\begin{bmatrix}R_f + sL_f & -\omega_N L_f\\ \omega_N L_f & R_f + sL_f\end{bmatrix}}^{\mathbf{Z}_f}\begin{bmatrix}\Delta i_{fd}^{\omega_N}\\ \Delta i_{fq}^{\omega_N}\end{bmatrix} \tag{8}$$

the small-signal model of the converter system in the dq^{ω_N} frame can be obtained in its conventional form as

$$\overbrace{\begin{bmatrix}\Delta i_{fd}^{\omega_N}\\ \Delta i_{fq}^{\omega_N}\end{bmatrix}}^{\mathbf{\Delta I}_f} = \mathbf{G}_c\begin{bmatrix}\Delta P_c^\star\\ \Delta E_g^\star\end{bmatrix} - \mathbf{Y}_c\overbrace{\begin{bmatrix}\Delta e_{gd}^{\omega_N}\\ \Delta e_{gq}^{\omega_N}\end{bmatrix}}^{\mathbf{\Delta E}_g} \tag{9}$$

where $\mathbf{Y}_c$ denotes the input-admittance[2] of the converter system seen from the PCC and is given by

$$\mathbf{Y}_c = [\mathbf{G}_T\mathbf{G}_{PVc2} + \mathbf{G}_{DH} - \mathbf{Z}_f]^{-1}[\mathbf{G}_T\mathbf{G}_{PVv2} - \mathbf{G}_{PVv1} - \mathbf{I}] \tag{10}$$

with $\mathbf{I}$ denoting the identity matrix of dimension 2×2.

As seen in (9), the input admittance characterizes the relationship between variations in the PCC voltage and variations in the converter current. In the dq^{ω_N} frame, $\Delta e_{gd}^{\omega_N}$ primarily reflects variations in the PCC voltage magnitude. Consequently, the elements $\mathbf{Y}_c(1,1)$ and $\mathbf{Y}_c(2,1)$ of the converter's input admittance describe the impact of PCC voltage magnitude variations on the converter current. Meanwhile, the effect of variations in the angular frequency of the PCC voltage on the converter current is represented in the dq^{ω_N} frame by the elements $\mathbf{Y}_c(1,2)$ and $\mathbf{Y}_c(2,2)$. This is because, in the dq^{ω_N} frame, variations in the angular frequency of the PCC voltage are primarily reflected in $\Delta e_{gq}^{\omega_N}$, as detailed in [39].

2) SMALL-SIGNAL MODELING OF INERTIAL GRID

To derive the small-signal model of the inertial grid, the source voltage vector, $\underline{e}_s^{\omega_s}$, in the source dq-frame (defined by the transformation angle, θ_s, which is obtained by integrating

[2] Since the direction of current flowing out of the converter in Fig. 1 is taken as positive, the negative sign for $\mathbf{Y}_c$ is used in (9).

the angular frequency of the voltage source, i.e., $\theta_s = \frac{\omega_s}{s}$) should be transformed to the dq^{ω_N} frame. By using the swing equation in (1), this transformation can be achieved from the following expression:

$$\underline{e}_s^{\omega_N} = \underline{e}_s^{\omega_s} e^{-j\theta'_L}, \quad \text{with} \quad \theta'_L = \theta_N - \theta_s = \frac{1}{s}\frac{G'_{pc}(P^\star_g - P_g)}{S_N}. \tag{11}$$

Linearizing (11), the small-signal model of the source voltage vector in the dq^{ω_N} frame can be expressed as

$$\begin{bmatrix}\Delta e_{sd}^{\omega_N}\\ \Delta e_{sq}^{\omega_N}\end{bmatrix} = \overbrace{\begin{bmatrix} e_{sq0}^{\omega_N} & 0\\ -e_{sd0}^{\omega_N} & 0\end{bmatrix}}^{\mathbf{G}_{e\theta}}\begin{bmatrix}\Delta\theta'_L\\ 0\end{bmatrix} + \overbrace{\begin{bmatrix}\cos\theta'_{L0} & \sin\theta'_{L0}\\ -\sin\theta'_{L0} & \cos\theta'_{L0}\end{bmatrix}}^{\mathbf{G}_{te}}\begin{bmatrix}\Delta e_{sd}^{\omega_s}\\ \Delta e_{sq}^{\omega_s}\end{bmatrix} \tag{12}$$

with

$$\begin{bmatrix}\Delta\theta'_L\\ 0\end{bmatrix} = \begin{bmatrix}\frac{G'_{pc}}{sS_N} & 0\\ 0 & 1\end{bmatrix}\begin{bmatrix}\Delta P^\star_g\\ 0\end{bmatrix} + \overbrace{\begin{bmatrix}-\frac{G'_{pc}e_{gd0}^{\omega_N}}{sS_N} & -\frac{G'_{pc}e_{gq0}^{\omega_N}}{sS_N}\\ 0 & 0\end{bmatrix}}^{\mathbf{G}_{\theta i}}\begin{bmatrix}\Delta i_{gd}^{\omega_N}\\ \Delta i_{gq}^{\omega_N}\end{bmatrix} + \overbrace{\begin{bmatrix}-\frac{G'_{pc}i_{gd0}^{\omega_N}}{sS_N} & -\frac{G'_{pc}i_{gq0}^{\omega_N}}{sS_N}\\ 0 & 0\end{bmatrix}}^{\mathbf{G}_{\theta e}}\begin{bmatrix}\Delta e_{gd}^{\omega_N}\\ \Delta e_{gq}^{\omega_N}\end{bmatrix} \tag{13}$$

where the expression $P_g = e_{gd}^{\omega_N} i_{gd}^{\omega_N} + e_{gq}^{\omega_N} i_{gq}^{\omega_N}$ is used for the active power injected into the grid. In (12), the transfer matrix $\mathbf{G}_{e\theta}$ describes the relationship between variations in the load angle of the voltage source and the source voltage vector in the dq^{ω_N} frame, while the matrix $\mathbf{G}_{te}$ relates variations in the magnitude of the source voltage to variations in the source voltage vector. Similar to (7), (13) describes the influence of active power variations at the PCC on the load angle of the voltage source. Since the magnitude of the source voltage is assumed constant, $\Delta e_{sd}^{\omega_s} = \Delta e_{sq}^{\omega_s} = 0$. By substituting (13) in (12) and using the linearized expression for the current dynamics in the dq^{ω_N} frame, which is given by

$$\begin{bmatrix}\Delta e_{sd}^{\omega_N}\\ \Delta e_{sq}^{\omega_N}\end{bmatrix} = \begin{bmatrix}\Delta e_{gd}^{\omega_N}\\ \Delta e_{gq}^{\omega_N}\end{bmatrix} - \overbrace{\begin{bmatrix}R_g + sL_g & -\omega_N L_g\\ \omega_N L_g & R_g + sL_g\end{bmatrix}}^{\mathbf{Z}_g}\begin{bmatrix}\Delta i_{gd}^{\omega_N}\\ \Delta i_{gq}^{\omega_N}\end{bmatrix} \tag{14}$$

the small-signal model of the inertial grid in the dq^{ω_N} frame can be obtained in its conventional form as

$$\overbrace{\begin{bmatrix}\Delta i_{gd}^{\omega_N}\\ \Delta i_{gq}^{\omega_N}\end{bmatrix}}^{\Delta\mathbf{I}_g} = \mathbf{G}_g\begin{bmatrix}\Delta P^\star_g\\ 0\end{bmatrix} + \mathbf{Y}_g\overbrace{\begin{bmatrix}\Delta e_{gd}^{\omega_N}\\ \Delta e_{gq}^{\omega_N}\end{bmatrix}}^{\Delta\mathbf{E}_g} \tag{15}$$

TABLE 1. System and Control Parameters for Considered System

System parameters		Control parameters	
S_N	1 kVA (1.0 pu)	H	5 s
E_N	100 V (1.0 pu)	K_D	50 pu
ω_N	314.16 rad/s (1.0 pu)	α_{vc}	$2\pi 1$ rad/s
R_f	0.015 pu	α_{hpf}	$2\pi 5$ rad/s
L_f	0.15 pu	R'_a	0.1 pu
R_g	0.02 pu	α_{lpf}	$2\pi 100$ rad/s
L_g	0.2 pu	α_{pc}	$2\pi 5$ rad/s

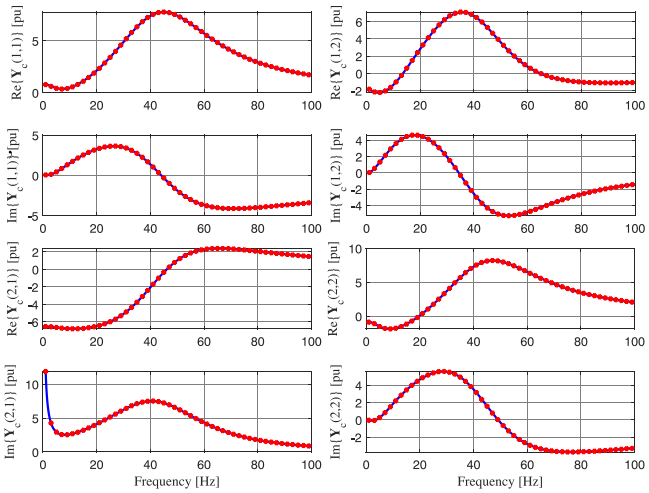

FIGURE 6. Frequency response of $\mathbf{Y}_c$; analytical model (solid-blue curves) and simulation model (dotted-red curves).

where $\mathbf{Y}_g$ denotes the input-admittance of the inertial grid seen from the PCC and is given by

$$\mathbf{Y}_g = [\mathbf{G}_{e\theta}\mathbf{G}_{\theta i} + \mathbf{Z}_g]^{-1}[\mathbf{I} - \mathbf{G}_{e\theta}\mathbf{G}_{\theta e}]. \tag{16}$$

3) VERIFICATION OF DERIVED SMALL-SIGNAL MODELS

To verify the analytically derived input admittance of the converter system and the inertial grid, detailed PSCAD/EMTDC time-domain simulation of the grid-connected converter system shown in Fig. 1 including all control loops (implemented in discrete time) is used. The dq^{ω_N} frame is aligned such that the d^{ω_N}-axis coincides with the PCC voltage vector in steady-state. Furthermore, independent dq-voltage perturbations are applied at the PCC to the individual subsystems at various frequencies. For each perturbation, the resulting perturbations in the dq-components of the current in the respective subsystem are measured, and the input admittance of each subsystem is extracted using discrete Fourier transform (DFT) calculations.

For all the simulation and experimental tests performed in this work, system and control parameters stated in Table 1 are used unless stated explicitly. Furthermore, the simulation tests are performed with the converter system injecting 0.8 pu active power and regulating the PCC voltage to 1.0 pu. Figs. 6 and 7 show the frequency response of the real and imaginary parts of the four elements of $\mathbf{Y}_c$ and $\mathbf{Y}_g$, respectively. The

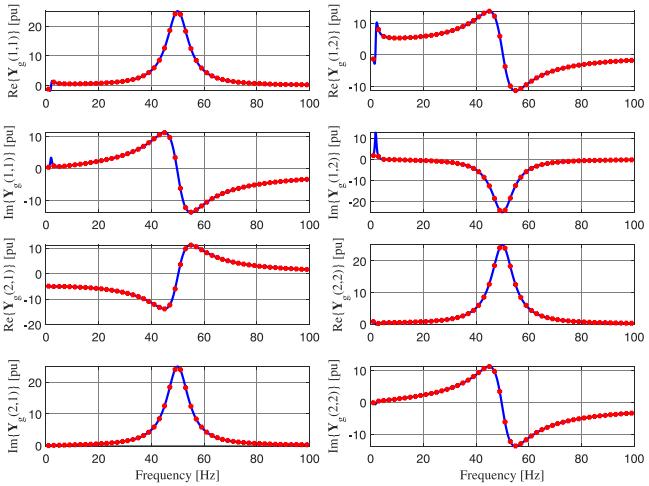

FIGURE 7. Frequency response of $\mathbf{Y_g}$; analytical model (solid-blue curves) and simulation model (dotted-red curves).

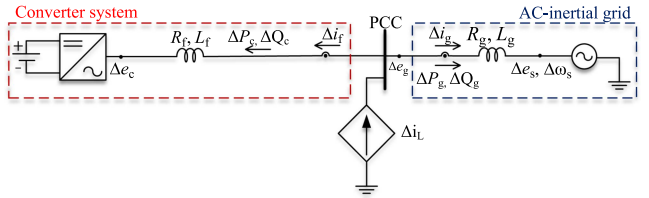

FIGURE 8. Applied disturbance to evaluate small-signal stability of grid-connected converter system.

results demonstrate a very good match between the analytical frequency characteristics and those obtained from simulations, verifying the validity of the analytical models.

4) DERIVATION OF SMALL-SIGNAL STABILITY ASSESSMENT CRITERION

To formulate an assessment criterion for evaluating the small-signal stability of the interconnected system, a shunt current perturbation, as depicted in Fig. 8, is considered as the source of disturbance. This disturbance results in variations in both the voltage magnitude and angular frequency at the PCC, which is reflected in terms of oscillations in both d- and q-components of the PCC voltage in the dq^{ω_N} frame. For the given disturbance, reference values for the active power and PCC voltage magnitude remain constant, which implies that $\Delta P_c^\star = \Delta P_g^\star = \Delta E_g^\star = 0$. By considering the current directions shown in Fig. 8 and using (9) and (15), an equivalent block-scheme (illustrated in Fig. 9) describing the small-signal characteristics of the grid-connected converter system in the dq^{ω_N} frame can be obtained. Accordingly, the small-signal stability of the system in this frame can be assessed by analyzing the poles of the closed-loop transfer matrix, $\mathbf{G}_{cl}^{\omega_N}$, which is given by

$$\frac{\mathbf{\Delta E_g}}{\mathbf{\Delta I_L}} = \mathbf{G}_{cl}^{\omega_N} = [\mathbf{I} + \mathbf{Y}_g^{-1}\mathbf{Y}_c]^{-1}\mathbf{Y}_g^{-1} \tag{17}$$

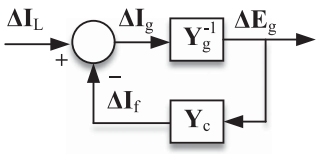

FIGURE 9. Equivalent block-scheme describing small-signal characteristics of grid-connected converter system in dq^{ω_N} frame.

where the matrix, $\mathbf{\Delta E_g}$, is as defined in (9) and $\mathbf{\Delta I_L} = \mathbf{\Delta I_f} + \mathbf{\Delta I_g}$.

B. SMALL-SIGNAL MODEL IN SYSTEM DQ-FRAME II

1) SMALL-SIGNAL MODELING OF CONVERTER SYSTEM

To derive the small-signal model of the converter system in the dq^{ω_g} frame, the controller dynamics should be transformed to this frame using the following relation:

$$\underline{z}^{\omega_g} = \underline{z}^{\omega_c} e^{j\delta_L}, \quad \text{with} \quad \delta_L = \theta_c - \theta_g. \tag{18}$$

Using linearized forms of (2), (3), and (18), the small-signal model of the converter voltage reference in the dq^{ω_g} frame can be expressed as

$$\begin{aligned}
\begin{bmatrix} \Delta e_{cd}^{\star\omega_g} \\ \Delta e_{cq}^{\star\omega_g} \end{bmatrix} &= \overbrace{\begin{bmatrix} -(e_{cq0}^{\omega_g} + G_{hpf}R'_a i_{fq0}^{\omega_g}) & G'_{vc}\cos\delta_{L0} \\ (e_{cd0}^{\omega_g} + G_{hpf}R'_a i_{fd0}^{\omega_g}) & G'_{vc}\sin\delta_{L0} \end{bmatrix}}^{\mathbf{G}'_T} \begin{bmatrix} \Delta\delta_L \\ \Delta E_g^\star \end{bmatrix} \\
&+ \left(- \overbrace{\begin{bmatrix} \frac{G_{vc}G_{lpf}\cos\delta_{L0}e_{gd0}^{\omega_g}}{E_{g0}} & \frac{G_{vc}G_{lpf}\cos\delta_{L0}e_{gq0}^{\omega_g}}{E_{g0}} \\ \frac{G_{vc}G_{lpf}\sin\delta_{L0}e_{gd0}^{\omega_g}}{E_{g0}} & \frac{G_{vc}G_{lpf}\sin\delta_{L0}e_{gq0}^{\omega_g}}{E_{g0}} \end{bmatrix}}^{\mathbf{G}'_{PVv1}} \right) \begin{bmatrix} \Delta e_{gd}^{\omega_g} \\ \Delta e_{gq}^{\omega_g} \end{bmatrix} \\
&+ \overbrace{\begin{bmatrix} -G_{hpf}R'_a & 0 \\ 0 & -G_{hpf}R'_a \end{bmatrix}}^{\mathbf{G}'_{DH}} \begin{bmatrix} \Delta i_{fd}^{\omega_g} \\ \Delta i_{fq}^{\omega_g} \end{bmatrix}
\end{aligned} \tag{19}$$

with

$$\begin{bmatrix} \Delta\delta_L \\ \Delta E_g^\star \end{bmatrix} = \begin{bmatrix} \frac{G_{pc}}{sS_N} & 0 \\ 0 & 1 \end{bmatrix} \begin{bmatrix} \Delta P_c^\star \\ \Delta E_g^\star \end{bmatrix}$$

$$\begin{aligned}
&+ \overbrace{\begin{bmatrix} -\frac{(G_{pc}+R_a)e_{gd0}^{\omega_g}}{sS_N} & -\frac{(G_{pc}+R_a)e_{gq0}^{\omega_g}}{sS_N} \\ 0 & 0 \end{bmatrix}}^{\mathbf{G}'_{PVc2}} \begin{bmatrix} \Delta i_{fd}^{\omega_g} \\ \Delta i_{fq}^{\omega_g} \end{bmatrix} \\
&+ \overbrace{\begin{bmatrix} -\frac{(G_{pc}+R_a)i_{fd0}^{\omega_g}}{sS_N} & -\frac{(G_{pc}+R_a)i_{fq0}^{\omega_g}}{sS_N} \\ 0 & 0 \end{bmatrix}}^{\mathbf{G}'_{PVv2}} \begin{bmatrix} \Delta e_{gd}^{\omega_g} \\ \Delta e_{gq}^{\omega_g} \end{bmatrix} \\
&- \overbrace{\begin{bmatrix} \frac{1}{s} & 0 \\ 0 & 0 \end{bmatrix}}^{\mathbf{G}'_{\delta\omega}} \begin{bmatrix} \Delta\omega_g \\ 0 \end{bmatrix}
\end{aligned} \tag{20}$$

where the expressions $P_c = e_{gd}^{\omega_g} i_{fd}^{\omega_g} + e_{gq}^{\omega_g} i_{fq}^{\omega_g}$, and $E_g = \sqrt{(e_{gd}^{\omega_g})^2 + (e_{gq}^{\omega_g})^2}$ are used for the active power output of the converter and the PCC-voltage magnitude, respectively.

Similar to (6), (19) describes the influence of variations in the converter load angle and set point for the AVC, PCC voltage, and converter current on the reference voltage of the converter. Furthermore, comparing (7) and (20) reveals that, unlike in the dq^{ω_N} frame, variations in the converter load angle in the dq^{ω_g} frame are influenced not only by active power variations but also by changes in the angular frequency of the PCC voltage. This influence is described by an additional transfer matrix, $\mathbf{G}'_{\delta\omega}$, in (20).

Again, by neglecting the impact of converter delays and using (19), (20), and the linearized expression for the current dynamics in the dq^{ω_g} frame, which is given by

$$\begin{bmatrix} \Delta e_{cd}^{\omega_g} \\ \Delta e_{cq}^{\omega_g} \end{bmatrix} = \begin{bmatrix} \Delta e_{gd}^{\omega_g} \\ \Delta e_{gq}^{\omega_g} \end{bmatrix} + \overbrace{\begin{bmatrix} R_f + sL_f & -\omega_N L_f \\ \omega_N L_f & R_f + sL_f \end{bmatrix}}^{\mathbf{Z}'_f} \begin{bmatrix} \Delta i_{fd}^{\omega_g} \\ \Delta i_{fq}^{\omega_g} \end{bmatrix} + \overbrace{\begin{bmatrix} -L_f i_{fq0}^{\omega_g} & 0 \\ L_f i_{fd0}^{\omega_g} & 0 \end{bmatrix}}^{\mathbf{G}'_{v\omega}} \begin{bmatrix} \Delta\omega_g \\ 0 \end{bmatrix} \tag{21}$$

the small-signal model of the converter system in the dq^{ω_g} frame is derived as

$$\begin{bmatrix} \Delta i_{fd}^{\omega_g} \\ \Delta i_{fq}^{\omega_g} \end{bmatrix} = \mathbf{G}'_c \begin{bmatrix} \Delta P_c^{\star} \\ \Delta E_g^{\star} \end{bmatrix} - \mathbf{Y}'_c \begin{bmatrix} \Delta e_{gd}^{\omega_g} \\ \Delta e_{gq}^{\omega_g} \end{bmatrix} - \mathbf{G}'_{ic\omega} \begin{bmatrix} \Delta\omega_g \\ 0 \end{bmatrix} \tag{22}$$

where $\mathbf{Y}'_c$ and $\mathbf{G}'_{ic\omega}$ are given by

$$\mathbf{Y}'_c = [\mathbf{G}'_T \mathbf{G}'_{PVc2} + \mathbf{G}'_{DH} - \mathbf{Z}'_f]^{-1} [\mathbf{G}'_T \mathbf{G}'_{PVv2} - \mathbf{G}'_{PVv1} - \mathbf{I}] \tag{23}$$

$$\mathbf{G}'_{ic\omega} = [\mathbf{G}'_T \mathbf{G}'_{PVc2} + \mathbf{G}'_{DH} - \mathbf{Z}'_f]^{-1} [\mathbf{G}'_{v\omega} + \mathbf{G}'_T \mathbf{G}'_{\delta\omega}]. \tag{24}$$

Comparing (10) and (23), it follows that the input admittance of the converter system is identical in both system dq-frames, i.e., $\mathbf{Y}_c = \mathbf{Y}'_c$, provided that the dq^{ω_N} and dq^{ω_g} frames are aligned in steady state. However, their physical interpretations differ. The elements $\mathbf{Y}'_c(1,1)$ and $\mathbf{Y}'_c(2,1)$ of the converter's input admittance describe the relationship between variations in the PCC voltage magnitude and the converter current in dq^{ω_g} frame, similar to dq^{ω_N} frame. However, the relationship between variations in the angular frequency of the PCC voltage and the converter current is modeled differently in the two system dq-frames. In the dq^{ω_g} frame, this relationship is modeled using an additional transfer matrix, $\mathbf{G}'_{ic\omega}$, rather than through the elements $\mathbf{Y}'_c(1,2)$ and $\mathbf{Y}'_c(2,2)$, as in dq^{ω_N} frame. This is because a small-signal disturbance resulting in voltage magnitude and angular frequency variations at the PCC does not affect the q-component of the PCC voltage vector in the dq^{ω_g} frame, since this frame is aligned to the PCC voltage. Thus, $\Delta e_{gq}^{\omega_g} = 0$.

2) SMALL-SIGNAL MODELING OF INERTIAL GRID

To derive the small-signal model of the inertial grid, the source voltage vector in the source dq-frame should be transformed to the dq^{ω_g} frame using the following expression:

$$\underline{e}_s^{\omega_g} = \underline{e}_s^{\omega_s} e^{-j\delta'_L}, \quad \text{with} \quad \delta'_L = \theta_g - \theta_s. \tag{25}$$

Linearizing (1) and (25), the small-signal model of the source voltage vector in the dq^{ω_g} frame can be expressed in its components form as

$$\begin{bmatrix} \Delta e_{sd}^{\omega_g} \\ \Delta e_{sq}^{\omega_g} \end{bmatrix} = \overbrace{\begin{bmatrix} e_{sq0}^{\omega_g} & 0 \\ -e_{sd0}^{\omega_g} & 0 \end{bmatrix}}^{\mathbf{G}'_{e\theta}} \begin{bmatrix} \Delta\delta'_L \\ 0 \end{bmatrix} + \overbrace{\begin{bmatrix} \cos\delta'_{L0} & \sin\delta'_{L0} \\ -\sin\delta'_{L0} & \cos\delta'_{L0} \end{bmatrix}}^{\mathbf{G}'_{te}} \begin{bmatrix} \Delta e_{sd}^{\omega_s} \\ \Delta e_{sq}^{\omega_s} \end{bmatrix} \tag{26}$$

with

$$\begin{bmatrix} \Delta\delta'_L \\ 0 \end{bmatrix} = \overbrace{\begin{bmatrix} \frac{1}{s} & 0 \\ 0 & 0 \end{bmatrix}}^{\mathbf{G}'_{\delta\omega}} \begin{bmatrix} \Delta\omega_g \\ 0 \end{bmatrix} + \begin{bmatrix} \frac{G'_{pc}}{sS_N} & 0 \\ 0 & 1 \end{bmatrix} \begin{bmatrix} \Delta P_g^{\star} \\ 0 \end{bmatrix} + \overbrace{\begin{bmatrix} -\frac{G'_{pc} e_{gd0}^{\omega_g}}{sS_N} & -\frac{G'_{pc} e_{gq0}^{\omega_g}}{sS_N} \\ 0 & 0 \end{bmatrix}}^{\mathbf{G}'_{\theta i}} \begin{bmatrix} \Delta i_{gd}^{\omega_g} \\ \Delta i_{gq}^{\omega_g} \end{bmatrix} + \overbrace{\begin{bmatrix} -\frac{G'_{pc} i_{gd0}^{\omega_g}}{sS_N} & -\frac{G'_{pc} i_{gq0}^{\omega_g}}{sS_N} \\ 0 & 0 \end{bmatrix}}^{\mathbf{G}'_{\theta e}} \begin{bmatrix} \Delta e_{gd}^{\omega_g} \\ \Delta e_{gq}^{\omega_g} \end{bmatrix} \tag{27}$$

where the expression $P_g = e_{gd}^{\omega_g} i_{gd}^{\omega_g} + e_{gq}^{\omega_g} i_{gq}^{\omega_g}$ is used for the active power injected into the grid.

Once again (27) reveals that, unlike in the dq^{ω_N} frame, variations in the load angle of the voltage source in the dq^{ω_g} frame are influenced not only by active power variations but also by changes in the angular frequency of the PCC voltage, which is described by transfer matrix, $\mathbf{G}'_{\delta\omega}$. Since the magnitude of the source voltage is assumed constant, $\Delta e_{sd}^{\omega_s} = \Delta e_{sq}^{\omega_s} = 0$. Finally, by substituting (27) in (26) and using the linearized expression for the current dynamics in the dq^{ω_g} frame, which is given by

$$\begin{bmatrix} \Delta e_{sd}^{\omega_g} \\ \Delta e_{sq}^{\omega_g} \end{bmatrix} = \begin{bmatrix} \Delta e_{gd}^{\omega_g} \\ \Delta e_{gq}^{\omega_g} \end{bmatrix} - \overbrace{\begin{bmatrix} R_g + sL_g & -\omega_N L_g \\ \omega_N L_g & R_g + sL_g \end{bmatrix}}^{\mathbf{Z}'_g} \begin{bmatrix} \Delta i_{gd}^{\omega_g} \\ \Delta i_{gq}^{\omega_g} \end{bmatrix} - \overbrace{\begin{bmatrix} -L_g i_{gq0}^{\omega_g} & 0 \\ L_g i_{gd0}^{\omega_g} & 0 \end{bmatrix}}^{\mathbf{G}'_{e\omega}} \begin{bmatrix} \Delta\omega_g \\ 0 \end{bmatrix} \tag{28}$$

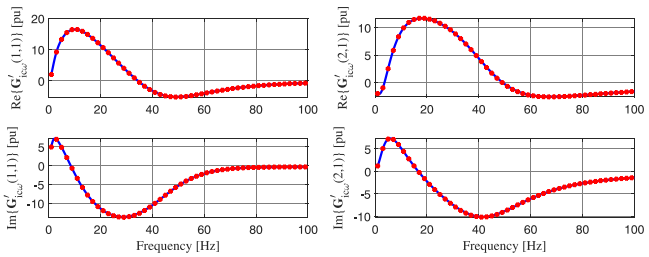

FIGURE 10. Frequency response of $\mathbf{G}'_{ic\omega}$; analytical model (solid-blue curves) and simulation model (dotted-red curves).

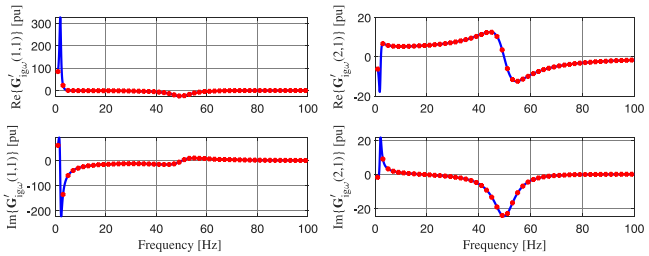

FIGURE 11. Frequency response of $\mathbf{G}'_{ig\omega}$; analytical model (solid-blue curves) and simulation model (dotted-red curves).

the small-signal model of the inertial grid in the dq^{ω_g} frame is derived as

$$\begin{bmatrix} \Delta i_{gd}^{\omega_g} \\ \Delta i_{gq}^{\omega_g} \end{bmatrix} = \mathbf{G}'_g \begin{bmatrix} \Delta P_g^{\star} \\ 0 \end{bmatrix} + \mathbf{Y}'_g \begin{bmatrix} \Delta e_{gd}^{\omega_g} \\ \Delta e_{gq}^{\omega_g} \end{bmatrix} + \mathbf{G}'_{ig\omega} \begin{bmatrix} \Delta\omega_g \\ 0 \end{bmatrix} \quad (29)$$

where $\mathbf{Y}'_g$ and $\mathbf{G}'_{ig\omega}$ are given by

$$\mathbf{Y}'_g = [\mathbf{G}'_{e\theta}\mathbf{G}'_{\theta i} + \mathbf{Z}'_g]^{-1}[\mathbf{I} - \mathbf{G}'_{e\theta}\mathbf{G}'_{\theta e}] \quad (30)$$

$$\mathbf{G}'_{ig\omega} = -[\mathbf{G}'_{e\theta}\mathbf{G}'_{\theta i} + \mathbf{Z}'_g]^{-1}[\mathbf{G}'_{e\omega} + \mathbf{G}'_{e\theta}\mathbf{G}'_{\delta\omega}]. \quad (31)$$

Similar to the input admittance of the converter system, it can be observed from (16) and (30) that the input admittance of the inertial grid in the two types of system dq-frames are equal, i.e., $\mathbf{Y}_g = \mathbf{Y}'_g$, if the dq^{ω_N} and dq^{ω_g} frames are aligned together in steady-state.

3) VERIFICATION OF THE DERIVED SMALL-SIGNAL MODELS

Since the input admittance of the converter system and inertial grid in the two system dq-frames are equal, results obtained from voltage perturbations in the dq^{ω_g} frame are not shown here. To verify $\mathbf{G}'_{ic\omega}$ and $\mathbf{G}'_{ig\omega}$ matrices, frequency perturbations are applied at the PCC to the individual subsystems at various frequencies and DFT calculations are performed. The results shown in Figs. 10 and 11 demonstrate a very good match between the analytical frequency characteristics and those obtained from simulations, verifying the validity of the analytical models.

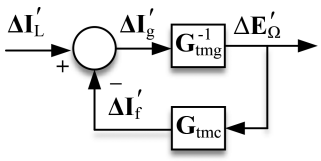

FIGURE 12. Equivalent block-scheme describing small-signal characteristics of grid-connected converter system in dq^{ω_g} frame.

4) DERIVATION OF SMALL-SIGNAL STABILITY ASSESSMENT CRITERION

As mentioned previously, since the dq^{ω_g} frame is aligned to the PCC voltage, a shunt current perturbation at the PCC (see Fig. 8), is reflected in terms of variations in the angular frequency and d-component of the PCC voltage vector only. This implies that for the given disturbance, all inputs other than $\Delta e_{gd}^{\omega_g}$ and $\Delta\omega_g$ in (22) and (29) are zero. By considering current directions, as shown in Fig. 8, the small-signal models of the converter system and inertial grid can be simplified for the given disturbance as follows:

$$\begin{bmatrix} \Delta i_{fd}^{\omega_g} \\ \Delta i_{fq}^{\omega_g} \end{bmatrix} = \mathbf{Y}'_c \begin{bmatrix} \Delta e_{gd}^{\omega_g} \\ 0 \end{bmatrix} + \mathbf{G}'_{ic\omega} \begin{bmatrix} \Delta\omega_g \\ 0 \end{bmatrix} \quad (32)$$

$$\begin{bmatrix} \Delta i_{gd}^{\omega_g} \\ \Delta i_{gq}^{\omega_g} \end{bmatrix} = \mathbf{Y}'_g \begin{bmatrix} \Delta e_{gd}^{\omega_g} \\ 0 \end{bmatrix} + \mathbf{G}'_{ig\omega} \begin{bmatrix} \Delta\omega_g \\ 0 \end{bmatrix}. \quad (33)$$

For convenience, (32) and (33) can be reformulated as

$$\overbrace{\begin{bmatrix} \Delta i_{fd}^{\omega_g} \\ \Delta i_{fq}^{\omega_g} \end{bmatrix}}^{\Delta\mathbf{I}'_f} = \overbrace{\begin{bmatrix} \mathbf{Y}'_c(1,1) & \mathbf{G}'_{ic\omega}(1,1) \\ \mathbf{Y}'_c(2,1) & \mathbf{G}'_{ic\omega}(2,1) \end{bmatrix}}^{\mathbf{G}_{tmc}} \overbrace{\begin{bmatrix} \Delta e_{gd}^{\omega_g} \\ \Delta\omega_g \end{bmatrix}}^{\Delta\mathbf{E}'_\Omega} \quad (34)$$

$$\overbrace{\begin{bmatrix} \Delta i_{gd}^{\omega_g} \\ \Delta i_{gq}^{\omega_g} \end{bmatrix}}^{\Delta\mathbf{I}'_g} = \overbrace{\begin{bmatrix} \mathbf{Y}'_g(1,1) & \mathbf{G}'_{ig\omega}(1,1) \\ \mathbf{Y}'_g(2,1) & \mathbf{G}'_{ig\omega}(2,1) \end{bmatrix}}^{\mathbf{G}_{tmg}} \overbrace{\begin{bmatrix} \Delta e_{gd}^{\omega_g} \\ \Delta\omega_g \end{bmatrix}}^{\Delta\mathbf{E}'_\Omega}. \quad (35)$$

It can be observed from (34) and (35) that unlike the dq-domain admittance/impedance, transfer matrices $\mathbf{G}_{tmc}$ and $\mathbf{G}_{tmg}$ provide a direct insight into the response of a subsystem during voltage magnitude and frequency variations. This formulation facilitates assessment of resonances [40], power system oscillation modes [29], as well as grid services (also referred to as GFM properties) offered by converter systems [39]. For instance, the $\mathbf{G}'_{ic\omega}(1,1)$ element in (34) can be used to assess the frequency-droop and inertial responses of the converter system, as it relates variations in the angular frequency of the PCC voltage to $\Delta i_{fd}^{\omega_g}$, which directly reflects active-power variations in the converter system [39].

By using (34) and (35), an equivalent block-scheme describing the small-signal characteristics of the grid-connected converter system in the dq^{ω_g} frame can be obtained, as illustrated in Fig. 12. Finally, the small-signal stability in this

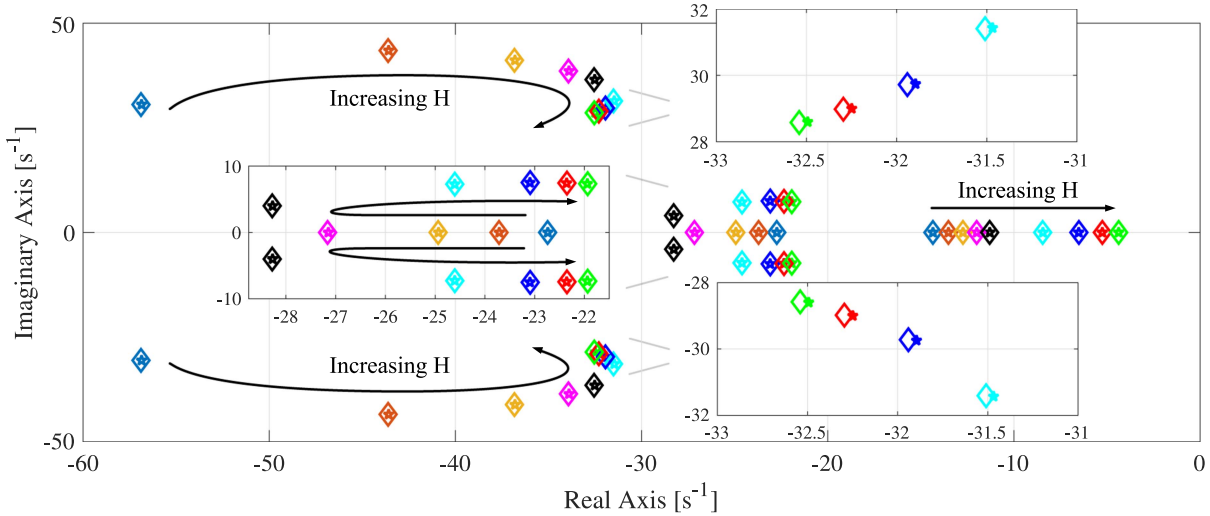

FIGURE 13. Poles of closed-loop transfer matrix $\mathbf{G}_{\mathrm{cl}}^{\omega_N}$ (depicted with star markers) and $\mathbf{G}_{\mathrm{cl}}^{\omega_g}$ (depicted with diamond markers) for various inertia time constant of grid. Direction of arrows depicts pole movement with increasing inertia time-constant.

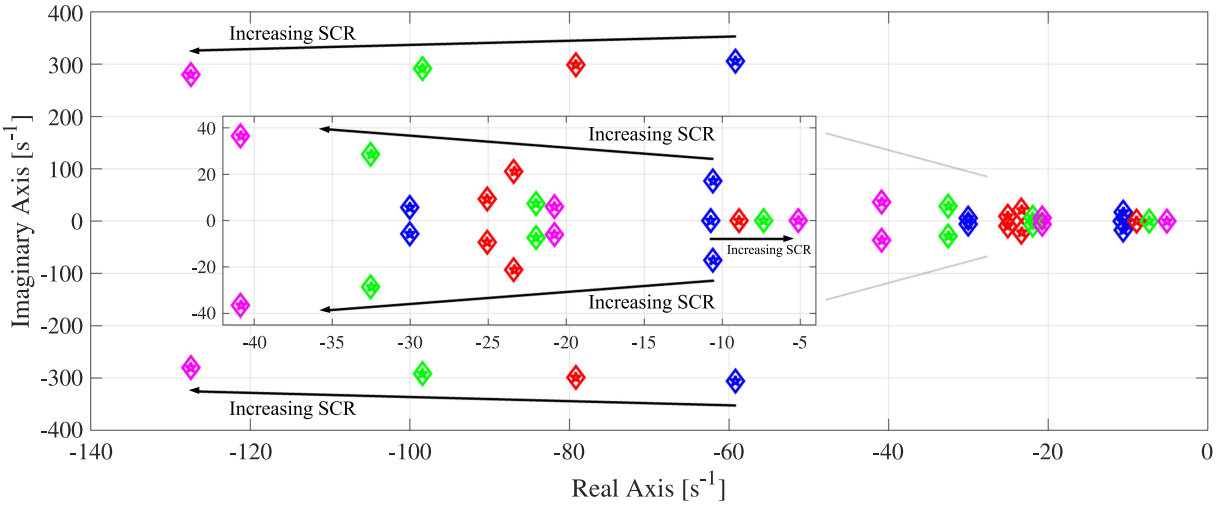

FIGURE 14. Poles of closed-loop transfer matrix $\mathbf{G}_{\mathrm{cl}}^{\omega_N}$ (depicted with star markers) and $\mathbf{G}_{\mathrm{cl}}^{\omega_g}$ (depicted with diamond markers) for four different values of SCR at PCC: 1.5 (blue), 3 (red), 5 (green), 10 (magenta). Direction of arrows depicts pole movement with increasing SCR.

frame can be assessed by analyzing the poles of the closed-loop transfer matrix, $\mathbf{G}_{\mathrm{cl}}^{\omega_g}$, which is given by

$$\frac{\Delta \mathbf{E}'_{\Omega}}{\Delta \mathbf{I}'_{\mathrm{L}}} = \mathbf{G}_{\mathrm{cl}}^{\omega_g} = [\mathbf{I} + \mathbf{G}_{\mathrm{tmg}}^{-1}\mathbf{G}_{\mathrm{tmc}}]^{-1}\mathbf{G}_{\mathrm{tmg}}^{-1} \tag{36}$$

where $\Delta \mathbf{I}'_{\mathrm{L}} = \Delta \mathbf{I}'_{\mathrm{f}} + \Delta \mathbf{I}'_{\mathrm{g}}$.

The analytical models derived in this section reveal that while small-signal modeling of a GFM converter system in dq^{ω_N} frame allows the use of conventional impedance/admittance-based models, as shown in (9) and (15), modeling in dq^{ω_g} frame, as presented in (34) and (35), provides deeper physical insights into the system's response during small disturbances. Due to the different open-loop transfer matrices in these two modeling approaches, the resulting closed-loop transfer matrices used to analyze the small-signal characteristics of an interconnected system differ between the two types of system dq-frames, as seen in (17) and (36). In the following section, these characteristics as assessed by both modeling approaches are compared.

V. COMPARISON OF SMALL-SIGNAL CHARACTERISTICS IN THE TWO SYSTEM *DQ* FRAMES

The small-signal characteristics of the grid-connected converter system, as assessed by the two modeling approaches discussed in the previous section, are compared here. To do so, the poles of the closed-loop transfer matrices, $\mathbf{G}_{\mathrm{cl}}^{\omega_N}$ in (17) and $\mathbf{G}_{\mathrm{cl}}^{\omega_g}$ in (36), are calculated and plotted in Fig. 13 , for various

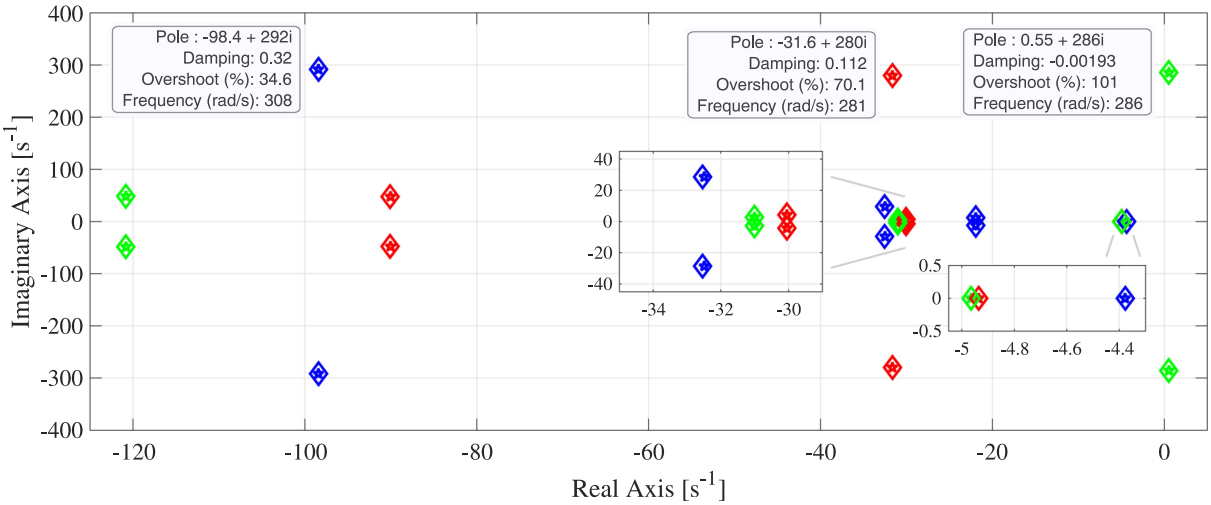

FIGURE 15. Poles of closed-loop transfer matrix $\mathbf{G}_{\mathrm{cl}}^{\omega_{\mathrm{N}}}$ (depicted with star markers) and $\mathbf{G}_{\mathrm{cl}}^{\omega_{\mathrm{g}}}$ (depicted with diamond markers) for three different values of loop-bandwidth of APC in converter system: $\alpha_{\mathrm{pc}} = 2\pi 5$ rad/s (blue), $\alpha_{\mathrm{pc}} = 2\pi 15$ rad/s (red), and $\alpha_{\mathrm{pc}} = 2\pi 20$ rad/s (green). An SCR = 5 is considered here.

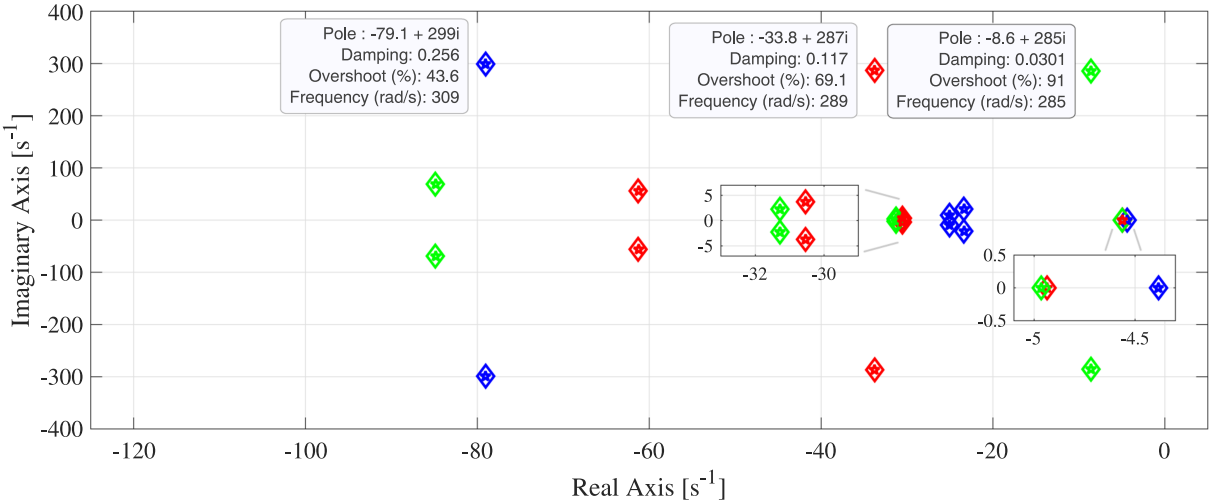

FIGURE 16. Poles of closed-loop transfer matrix $\mathbf{G}_{\mathrm{cl}}^{\omega_{\mathrm{N}}}$ (depicted with star markers) and $\mathbf{G}_{\mathrm{cl}}^{\omega_{\mathrm{g}}}$ (depicted with diamond markers) for three different values of loop-bandwidth of APC in converter system: $\alpha_{\mathrm{pc}} = 2\pi 5$ rad/s (blue), $\alpha_{\mathrm{pc}} = 2\pi 15$ rad/s (red), and $\alpha_{\mathrm{pc}} = 2\pi 20$ rad/s (green). An SCR = 3 is considered here.

inertia time-constant H of the grid. As shown in the figure, both closed-loop transfer matrices share essentially the same poles (apart from a small offset that arises due to numerical inconsistency in obtaining the poles), indicating that the two modeling approaches yield identical information regarding the small-signal characteristics of the system, regardless of its frequency strength.[3]

Furthermore, Fig. 14 presents the poles of $\mathbf{G}_{\mathrm{cl}}^{\omega_{\mathrm{N}}}$ and $\mathbf{G}_{\mathrm{cl}}^{\omega_{\mathrm{g}}}$, for four different values of grid impedance, corresponding to short-circuit ratios (SCR) of 1.5 (blue), 3 (red), 5 (green), and 10 (magenta) at the PCC. Again, the figure shows that both modeling approaches provide consistent information about the small-signal characteristics of the system, regardless of the grid strength at the converter's connection point.

Finally, Figs. 15 and 16 illustrate the poles of $\mathbf{G}_{\mathrm{cl}}^{\omega_{\mathrm{N}}}$ and $\mathbf{G}_{\mathrm{cl}}^{\omega_{\mathrm{g}}}$ for three different loop bandwidths of the APC in the converter system: $\alpha_{\mathrm{pc}} = 2\pi 5$ rad/s (blue), $\alpha_{\mathrm{pc}} = 2\pi 15$ rad/s (red), and $\alpha_{\mathrm{pc}} = 2\pi 20$ rad/s (green), considering an SCR of 5 and 3 at the PCC, respectively. These figures confirm that both modeling approaches provide the same conclusion regarding the system's small-signal characteristics. Moreover, a comparison of the dominant poles for $\alpha_{\mathrm{pc}} = 2\pi 20$ rad/s (green) in Figs. 15 and 16 reveals that an SCR of 5 leads to small-signal instability, as indicated by the presence of poles with positive real parts. In contrast, an SCR of three results in stable system operation. This aligns with the findings in [35], which highlight the limitation on the maximum bandwidth

[3] Higher system inertia corresponds to higher frequency strength, and vice versa.

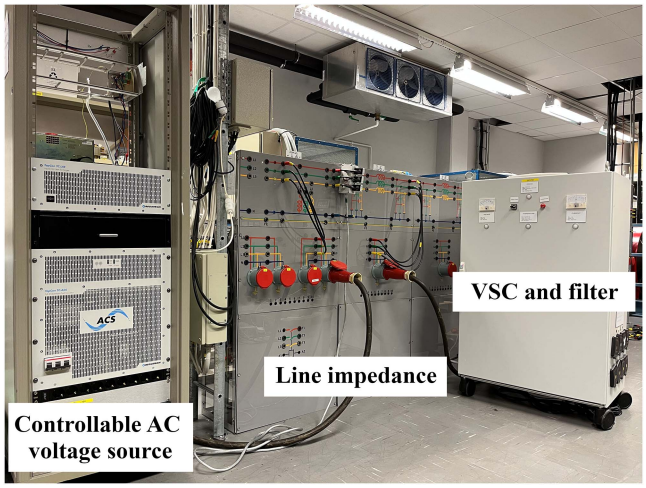

FIGURE 17. Photograph of laboratory setup.

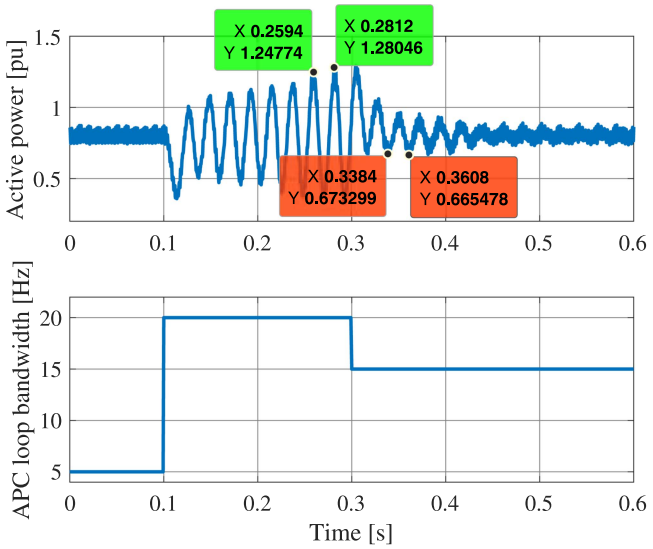

FIGURE 18. Impact of APC's loop bandwidth on active power response of system. An SCR = 5 is considered here.

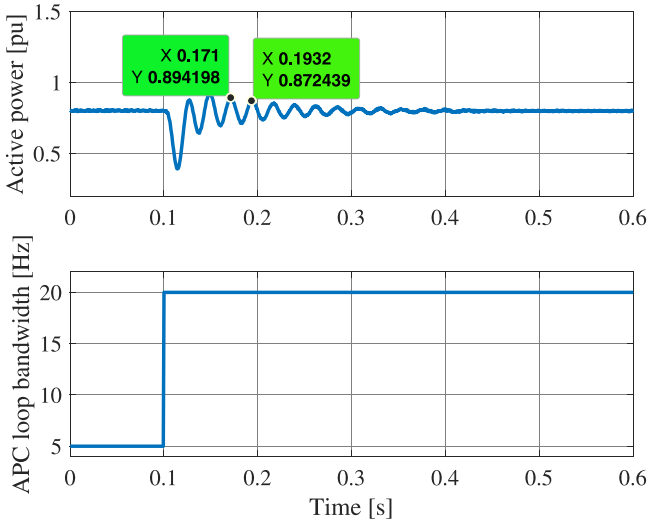

FIGURE 19. Impact of APC's loop bandwidth on active power response of system. An SCR = 3 is considered here.

selection for the APC when using the chosen type of GFM control under strong grid conditions.

The analysis in this section demonstrates that, despite having different closed-loop transfer matrices, both modeling approaches provide identical information regarding the small-signal characteristics of the grid-connected converter system. While the modeling approach in dq^{ω_N} frame allows for the use of conventional impedance/admittance-based models, the modeling approach in dq^{ω_g} frame enables a direct assessment of GFM properties in converter systems and offers deeper physical insights into system behavior during small disturbances, as previously highlighted.

VI. EXPERIMENTAL VALIDATION OF THE STABILITY ASSESSMENT

In order to validate the correctness of the analytical model, experimental validation is made and discussed in this section. A photo of the laboratory setup is depicted in Fig. 17 and it resembles the system shown in Fig. 1. The grid is emulated using an REGATRON's four quadrant programmable ac power source. Furthermore, the GFM converter system used here comprises of a two-level VSC supplied by an ideal dc voltage source. It is controlled using dSPACE dS1006, and is connected at the PCC through a phase reactor of resistance R_f and inductance L_f. The experiment is performed using the same operating points mentioned earlier and the system and control parameters specified in Table 1.

The impact of the APC loop bandwidth on the small-signal stability of the converter system is analyzed for two different grid strengths, corresponding to an SCR of 5 and 3 at the PCC. For the first case, where the SCR is 5 at the PCC, a step change in α_{pc} is introduced, as shown in Fig. 18. From the figure, it is evident that undamped oscillations commence in the active power output of the converter system at $t = 0.1$ s, when the APC loop bandwidth is increased to $2\pi 20$ rad/s. This change leads to system instability, consistent with the theoretical analysis in the previous section. Furthermore, the angular frequency of these undamped oscillations (≈ 288 rad/s) closely aligns with the angular frequency of the unstable pole shown in Fig. 15 for this configuration. In addition, by reducing α_{pc} to $2\pi 15$ rad/s at $t = 0.3$ s, the active power output of the converter system stabilizes after a poorly damped oscillatory response at around 281 rad/s, closely matching the angular frequency of the dominant pole depicted in Fig. 15 for this case.

For the second case, where the SCR is 3 at the PCC, Fig. 19 shows that increasing the APC bandwidth to $2\pi 20$ rad/s does not result in small-signal instability, aligning with the above-mentioned theoretical analysis. Furthermore, the angular frequency of the poorly damped oscillations (≈ 283 rad/s) closely matches with that of the dominant pole depicted in Fig. 16 for this case. Minor discrepancies between the predicted and actual angular frequencies of the oscillations in

both cases can be attributed to inaccuracies in the experimental model parameters, such as the filter inductance and resistance.

These experimental results thus confirm the correctness and accuracy of the small-signal models.

VII. CONCLUSION

This article presents a comparative evaluation of small-signal modeling for GFM converter systems in two distinct system dq-frames: one defined by the system's rated angular frequency and the other by its fundamental angular frequency. A step-by-step derivation of the small-signal models is provided, and analytical results are used to demonstrate the equivalency of these two modeling approaches across various scenarios. It is shown that, while small-signal modeling in dq^{ω_N} frame enables the use of conventional impedance/admittance-based models, modeling in dq^{ω_g} frame provides deeper physical insights into converter system dynamics during small grid disturbances, including variations in grid voltage magnitude and frequency. In addition, this approach allows a direct assessment of frequency-droop and inertial responses. Assessment of these responses are increasingly demanded by system operators to evaluate frequency stability and the GFM properties of converter systems. Finally, experiments are conducted to validate the accuracy of the analytical results. Measurements show that the angular frequency of oscillations and the small-signal stability of the studied GFM converter system closely align with predictions from the analytical models.

ACKNOWLEDGMENT

In particular, the authors acknowledge Hitachi Energy, Svenska kraftnät, and DNV for their contribution and support to the project.

REFERENCES

[1] J. Shair, H. Li, J. Hu, and X. Xie, "Power system stability issues, classifications and research prospects in the context of high-penetration of renewables and power electronics," *Renewable Sustain. Energy Rev.*, vol. 145, 2021, Art. no. 111111. [Online]. Available: https://www.sciencedirect.com/science/article/pii/S1364032121003993

[2] N. Hatziargyriou et al., "Definition and classification of power system stability–revisited & extended," *IEEE Trans. Power Syst.*, vol. 36, no. 4, pp. 3271–3281, Jul. 2021.

[3] G. Pinares and M. Bongiorno, "Modeling and analysis of VSC-based HVDC systems for DC network stability studies," *IEEE Trans. Power Del.*, vol. 31, no. 2, pp. 848–856, Apr. 2016.

[4] M. Amin and M. Molinas, "Small-signal stability assessment of power electronics based power systems: A discussion of impedance- and eigenvalue-based methods," *IEEE Trans. Ind. Appl.*, vol. 53, no. 5, pp. 5014–5030, Sep./Oct. 2017.

[5] M. Amin, J. A. Suul, S. D'Arco, E. Tedeschi, and M. Molinas, "Impact of state-space modelling fidelity on the small-signal dynamics of VSC-HVDC systems," in *Proc. IET Int. Conf. AC DC Power Transmiss.*, 2015, pp. 1–11.

[6] N. Pogaku, M. Prodanovic, and T. C. Green, "Modeling, analysis and testing of autonomous operation of an inverter-based microgrid," *IEEE Trans. Power Electron.*, vol. 22, no. 2, pp. 613–625, Mar. 2007.

[7] X. Wang and F. Blaabjerg, "Harmonic stability in power electronic-based power systems: Concept, modeling, and analysis," *IEEE Trans. Smart Grid*, vol. 10, no. 3, pp. 2858–2870, May 2019.

[8] X. Wang, F. Blaabjerg, and W. Wu, "Modeling and analysis of harmonic stability in an AC power-electronics-based power system," *IEEE Trans. Power Electron.*, vol. 29, no. 12, pp. 6421–6432, Dec. 2014.

[9] Y. Tan, Y. Sun, J. Lin, L. Yuan, and M. Su, "Revisit impedance-based stability analysis of VSC-HVDC system," *IEEE Trans. Power Syst.*, vol. 39, no. 1, pp. 1728–1738, Jan. 2024.

[10] L. Xiong, X. Liu, Y. Liu, and F. Zhuo, "Modeling and stability issues of voltage-source converter-dominated power systems: A review," *CSEE J. Power Energy Syst.*, vol. 8, no. 6, pp. 1530–1549, Nov. 2022.

[11] X. Wang, L. Harnefors, and F. Blaabjerg, "Unified impedance model of grid-connected voltage-source converters," *IEEE Trans. Power Electron.*, vol. 33, no. 2, pp. 1775–1787, Feb. 2018.

[12] L. Fan and Z. Miao, "Admittance-based stability analysis: Bode plots, Nyquist diagrams or eigenvalue analysis?," *IEEE Trans. Power Syst.*, vol. 35, no. 4, pp. 3312–3315, Jul. 2020.

[13] Y. Xu, Z. Gu, and K. Sun, "Characterization of subsynchronous oscillation with wind farms using describing function and generalized Nyquist criterion," *IEEE Trans. Power Syst.*, vol. 35, no. 4, pp. 2783–2793, Jul. 2020.

[14] M. Beza and M. Bongiorno, "Identification of resonance interactions in offshore-wind farms connected to the main grid by MMC-based HVDC system," *Int. J. Elect. Power Energy Syst.*, vol. 111, pp. 101–113, 2019. [Online]. Available: https://www.sciencedirect.com/science/article/pii/S0142061518324013

[15] B. Wen, D. Boroyevich, R. Burgos, P. Mattavelli, and Z. Shen, "Analysis of D-Q small-signal impedance of grid-tied inverters," *IEEE Trans. Power Electron.*, vol. 31, no. 1, pp. 675–687, Jan. 2016.

[16] G. Wu et al., "Passivity-based stability analysis and generic controller design for grid-forming inverter," *IEEE Trans. Power Electron.*, vol. 38, no. 5, pp. 5832–5843, May 2023.

[17] F. Zhao, X. Wang, and T. Zhu, "Low-frequency passivity-based analysis and damping of power-synchronization controlled grid-forming inverter," *IEEE Trans. Emerg. Sel. Topics Power Electron.*, vol. 11, no. 2, pp. 1542–1554, Apr. 2023.

[18] M. Beza and M. Bongiorno, "Impact of converter control strategy on low- and high-frequency resonance interactions in power-electronic dominated systems," *Int. J. Elect. Power Energy Syst.*, vol. 120, 2020, Art. no. 105978.

[19] M. Beza and M. Bongiorno, "On the risk for subsynchronous control interaction in type 4 based wind farms," *IEEE Trans. Sustain. Energy*, vol. 10, no. 3, pp. 1410–1418, Jul. 2019.

[20] L. Harnefors, X. Wang, A. G. Yepes, and F. Blaabjerg, "Passivity-based stability assessment of grid-connected VSCs—an overview," *IEEE Trans. Emerg. Sel. Topics Power Electron.*, vol. 4, no. 1, pp. 116–125, Mar. 2016.

[21] L. Harnefors, M. Bongiorno, and S. Lundberg, "Input-admittance calculation and shaping for controlled voltage-source converters," *IEEE Trans. Ind. Electron.*, vol. 54, no. 6, pp. 3323–3334, Dec. 2007.

[22] W. Du, B. Ren, H. Wang, and Y. Wang, "Comparison of methods to examine sub-synchronous oscillations caused by grid-connected wind turbine generators," *IEEE Trans. Power Syst.*, vol. 34, no. 6, pp. 4931–4943, Nov. 2019.

[23] L. Sainz, M. Cheah-Mane, L. Monjo, J. Liang, and O. Gomis-Bellmunt, "Positive-net-damping stability criterion in grid-connected VSC systems," *IEEE Trans. Emerg. Sel. Topics Power Electron.*, vol. 5, no. 4, pp. 1499–1512, Dec. 2017.

[24] G. Stamatiou and M. Bongiorno, "Stability analysis of two-terminal VSC-HVDC systems using the net-damping criterion," *IEEE Trans. Power Del.*, vol. 31, no. 4, pp. 1748–1756, Aug. 2016.

[25] L. Harnefors, "Proof and application of the positive-net-damping stability criterion," *IEEE Trans. Power Syst.*, vol. 26, no. 1, pp. 481–482, Feb. 2011.

[26] J. Yu, S. Wang, Z. Liu, J. Li, J. Liu, and J. Shang, "Accurate small-signal terminal characteristic model and SISO stability analysis approach for parallel grid-forming inverters in islanded microgrids," *IEEE Trans. Power Electron.*, vol. 38, no. 5, pp. 6597–6612, May 2023.

[27] W. Cao, Y. Ma, F. Wang, L. M. Tolbert, and Y. Xue, "Low-frequency stability analysis of inverter-based islanded multiple-bus AC microgrids based on terminal characteristics," *IEEE Trans. Smart Grid*, vol. 11, no. 5, pp. 3662–3676, Sep. 2020.

[28] S. Wang, Z. Liu, J. Liu, D. Boroyevich, and R. Burgos, "Small-signal modeling and stability prediction of parallel droop-controlled inverters based on terminal characteristics of individual inverters," *IEEE Trans. Power Electron.*, vol. 35, no. 1, pp. 1045–1063, Jan. 2020.

[29] S. Shah, W. Yan, V. Gevorgian, and W. Gao, "Power-domain impedance theory for the analysis and mitigation of interarea oscillations," in *Proc. IEEE Power Energy Soc. Gen. Meeting*, 2020, pp. 1–5.
[30] F. Cavazzana, A. Khodamoradi, H. Abedini, and P. Mattavelli, "Analysis of an impedance modeling approach for droop-controlled inverters in system DQ frame," in 2019 *Proc. IEEE Energy Convers. Congr. Expo.*, 2019, pp. 5576–5583.
[31] Z. Liu, J. Liu, D. Boroyevich, and R. Burgos, "Stability criterion of droop-controlled parallel inverters based on terminal-characteristics of individual inverters," in *Proc. IEEE 8th Int. Power Electron. Motion Control Conf.*, 2016, pp. 2958–2963.
[32] Z. Liu, J. Liu, D. Boroyevich, R. Burgos, and T. Liu, "Small-signal terminal-characteristics modeling of three-phase droop-controlled inverters," in *Proc. IEEE Energy Convers. Congr. Expo.*, 2016, pp. 1–7.
[33] P. Kundur, N. Balu, and M. Lauby, *Power System Stability and Control* (EPRI Power System Engineering Series). New York, NY, USA: McGraw-Hill, 1994.
[34] A. Narula, "Grid-forming wind power plants," Ph.D. dissertation, Dept. of Elect. Eng., Chalmers Univ. Technol., Göteborg, Sweden, 2023.
[35] L. Harnefors, M. Hinkkanen, U. Riaz, F. M. M. Rahman, and L. Zhang, "Robust analytic design of power-synchronization control," *IEEE Trans. Ind. Electron.*, vol. 66, no. 8, pp. 5810–5819, Aug. 2019.
[36] L. Zhang, L. Harnefors, and H.-P. Nee, "Power-synchronization control of grid-connected voltage-source converters," *IEEE Trans. Power Syst.*, vol. 25, no. 2, pp. 809–820, May 2010.
[37] J. Sun, "Impedance-based stability criterion for grid-connected inverters," *IEEE Trans. Power Electron.*, vol. 26, no. 11, pp. 3075–3078, Nov. 2011.
[38] H. Liu, X. Xie, and W. Liu, "An oscillatory stability criterion based on the unified dq-frame impedance network model for power systems with high-penetration renewables," *IEEE Trans. Power Syst.*, vol. 33, no. 3, pp. 3472–3485, May 2018.
[39] A. Narula, P. Imgart, M. Bongiorno, P. Mattavelli, M. Beza, and J. R. Svensson, "Power-response matrix-based modeling of converter systems for small-signal analysis," in *Proc. IEEE Energy Convers. Congr. Expo.*, 2024, pp. 1–8.
[40] S. Liu, H. Wu, X. Wang, T. Bosma, and G. Sauba, "Stability analysis and active damping design for grid-forming converters in LC resonant grids," *IEEE Open J. Ind. Electron. Soc.*, vol. 5, pp. 143–154, 2024.

ANANT NARULA (Member, IEEE) received the M.Sc. degree in smart electrical networks and systems (EIT InnoEnergy) from the KTH Royal Institute of Technology, Stockholm, Sweden, and the Universitat Politècnica de Catalunya, Barcelona, Spain, in 2018, and the Ph.D. degree in electric power engineering from the Chalmers University of Technology, Göteborg, Sweden, in 2023.

He is currently a Postdoctoral Researcher with the Chalmers University of Technology. His research interests include the applications of power electronics in power systems, converter control, and stability studies of power systems.

MASSIMO BONGIORNO (Senior Member, IEEE) received the M.Sc. degree in electrical engineering from the University of Palermo, Palermo, Italy, in 2002, and the Lic. Eng. and Ph.D. degrees in electric power engineering from the Chalmers University of Technology, Gothenburg, Sweden, in 2004 and 2007, respectively.

From 2007 to 2010, he was an Assistant Professor with the Department of Electric Power Engineering, Chalmers University of Technology, where he became an Associate Professor in 2010. Since 2015, he has been a Professor in power electronic applications for power systems, and since 2020 he is the Head of the Division of Electric Power Engineering, Chalmers University of Technology. Since 2022, he has been the Director of the centre of excellence The Swedish Electricity Storage and Balancing Centre, Chalmers University of Technology. His research interests include the application of power electronics in power systems, converter control, power system dynamics, and power quality.

PAOLO MATTAVELLI (Fellow, IEEE) received the M.S. (Hons.) and Ph.D. degrees in electrical engineering from the University of Padova, Padova, Italy, in 1992 and 1995, respectively.

He is currently a Full Professor in electronics with the University of Padova. His current Google scholar H-index is 90. His research interests include analysis, modeling, and control of power converters, grid-connected converters for renewable energy systems and microgrids, and high-temperature and high-power-density power electronics.

Dr. Mattavelli was a recipient of the Prize Paper Award in IEEE TRANSACTIONS ON POWER ELECTRONICS in 2005, 2006, 2011, and 2012, and the 2nd Prize Paper Award at the IEEE Industry Applications Society Annual Meeting in 2007. From 2003 to 2012, he was an Associate Editor for IEEE TRANSACTIONS ON POWER ELECTRONICS. From 2018 to 2024, he was a Co-Editor-in-Chief for IEEE TRANSACTIONS ON POWER ELECTRONICS. From 2005 to 2010, he was the Industrial Power Converter Committee Technical Review Chair for IEEE TRANSACTIONS ON INDUSTRY APPLICATIONS. From 2003 to 2006, 2006 to 2009, and 2013 to 2015, he was a Member-At-Large of the IEEE Power Electronics Society's Administrative Committee.

MEBTU BEZA (Member, IEEE) received the B.Sc. degree in electrical engineering from Bahir Dar University, Bahir Dar, Ethiopia, in July 2005, and the M.Sc., Lic.Eng., and Ph.D. degrees in electric power engineering from the Chalmers University of Technology, Gothenburg, Sweden, in 2009, 2012, and 2015, respectively, and the D.Sc. degree (Docent) in control and modeling of power electronic converters in power systems from the Chalmers University of Technology, in 2020.

He is currently an Associate Professor with the Chalmers University of Technology. His research interests include signal processing in power systems, control theory, stability studies in converter-dominated systems, converter topologies and application of power electronics in power systems.

JAN R. SVENSSON (Senior Member, IEEE) received the Ph.D. and D.Sc. degrees (Docent) in electric power engineering from the Chalmers University of Technology, Göteborg, Sweden, in 1988 and 2002 respectively.

From 1999 to 2009, he was with ABB in R&D of HVDC Transmission, STATCOMs, and energy storages, especially design and control of light-concept devices (HVDC and FACTS). Between 2009 and 2014, he was the Program Manager for the Global R&D Program "Active Grid Infrastructure" with ABB Corporate Research. From 2014 to 2020, he was a Senior Principal Scientist on power electronics systems with ABB Power Grids Research. In addition to his current role as a Research Fellow with Hitachi Energy Research, Västerås, Sweden, he has also been an Adjunct Professor with the Chalmers University of Technology since 2018. His research interests include design and control of power electronics in power systems, power quality, storage technologies, and renewable energy.

WENTAO LIU (Member, IEEE) received the B.S. degree in electrical engineering and automation and the M.S. degree in electrical engineering from Shandong University, Jinan, China, in 2018 and 2020, respectively, and the Ph.D. degree in power electronics from AAU Energy, Aalborg University, Aalborg, Denmark in 2024.

He is currently a Postdoctoral Researcher with the Department of Electric Power Engineering, Chalmers University of Technology, Gothenburg, Sweden. His research interests include the modeling and control of grid-forming converters, grid stability assessment, grid impedance estimation, and wide bandgap power devices.